Open-Loop Control of Soft Hydrogel Microrobot Swarms for Targeted Thrombolysis in a Preclinical Model

Simone Schuerle

simone.schuerle@hest.ethz.ch

Swiss Federal Institute of Technology in Zurich https://orcid.org/0000-0001-5693-1603

Yimo Yan

ETH Zurich

Josh Mosfin

ETH Zurich

Tim Grossrieder

ETH Zurich https://orcid.org/0009-0009-8050-4834

Gian-Andrea Burkard

ETH Zurich

Archit Mundada

ETH Zurich

Myungjin Park

ETH Zurich

Laurensz Moeharram

ETH Zurich

Zaiyi Shen

Peking University

Dongfang Fu

Peking University

Louise Gillon

ETH Zurich

Petra Wollint

ETH Zurich

Christian Stoeck

ETH Zurich

Jianbo Tang

ETH Zurich

Etienne Geistlich

ETH Zurich
Arthur Vermeersch
ETH Zurich
Stella Morger
ETH Zurich
Nikola Cesarovic
ETH Zurich

Article

Keywords:

Posted Date: March 9th, 2026

DOI: https://doi.org/10.21203/rs.3.rs-8923535/v1

Additional Declarations: Yes there is potential Competing Interest. Simone Schuerle is co-founder and member of the board of Magnebotix AG.

Open-Loop Control of Soft Hydrogel Microrobot Swarms for Targeted Thrombolysis in a Preclinical Model

Yimo Y. Yan[1,#], Joshua M. Mesfin[1,2,#], Tim Grossrieder[1], Gian-Andrea Burkard[1], Archit Mundada[1], Myungjin Park[1], Laurensz Moeharram[1], Zaiyi Shen[3], Dongfang Fu[3], Louise Gillion[1], Petra Wolint[2], Christian T. Stoeck[4], Jianbo Tang[1], Etienne Geistlich[1], Arthur Vermeersch[1], Stella Morger[1], Nikola Cesarovic[2,5,6], Simone Schuerle[1,*]

1 Institute of Robotics and Intelligent Systems, Department of Health Sciences and Technology, ETH Zurich, 8092 Zurich, Switzerland

2 Institute of Translational Medicine, Department of Health Sciences and Technology, ETH Zurich, 8092 Zurich, Switzerland

3 State Key Laboratory for Turbulence and Complex Systems, School of Mechanics and Engineering Science, Peking University, Beijing, China

4 Center for Preclinical Development, University Hospital of Zurich, University of Zurich, Zurich, Switzerland

5 Deutsches Herzzentrum der Charité (DHZC), Department of Cardiothoracic and Vascular Surgery, Berlin, Germany

6 Charité – Universitätsmedizin Berlin, corporate member of Freie Universität Berlin and Humboldt-Universität zu Berlin and Berlin Institute of Health, Berlin, Germany

[#] These authors contributed equally and are listed in no particular order, to be regarded as co-first authors.

*Corresponding author: Simone Schuerle

Abstract

Thrombosis treatments, such as systemic administration of thrombolytics, suffer from poor efficacy and increased remaining-thrombus burden, resulting from a no-reflow zone adjacent to thrombi. Here we present the use of a magnetically guidable soft hydrogel microrobotic device, our HydroBots, which are comprised of a dextran shell and iron oxide nanoparticles chains. Their anisotropic shape and small size (10 μm) allow for ease of maneuverability to thus deliver systemic thrombolytics to break down thrombi. Computational models of the no-reflow region demonstrate HydroBots can navigate into the no-reflow region for effective drug delivery. *In vitro* tests show biocompatibility, hemocompatibility, and lack of immunogenicity for the HydroBots. Further *in vitro* tests reflect enhanced efficacy of thrombolytics with HydroBot administration compared to exclusive tPA injection. Finally, we perform *in vivo* tests in a thrombus-occluded porcine renal artery. Across various tissue plasminogen activator (tPA) doses, much lower than the total dose administered clinically, the HydroBots-tPA combination achieves better recanalization compared to tPA administration alone. Here, through safety and enhanced efficacy, our HydroBot demonstrates clinical promise as a novel solution for convection-enhanced thrombolytic drug delivery.

Introduction

Cardiovascular disease (CVD) has remained a leading global health challenge for decades, often involving blood vessel obstruction due to pathological blood clot formation[1]. These obstructions are often triggered by endothelial damage, can cause vessel blockage, called no-reflow regions[1, 2], and can have systemic consequences[3]. To treat thrombus formation, systemic administration of fibrinolytics, such as urokinase, streptokinase, and tPA, are used as standard of care worldwide[4]. However, thrombolytic agents face challenges reaching occluded sites due to the no-reflow region, increasing diffusion resistance from drug-bearing blood flow to the thrombus and thus reducing drug access[5]. As a result, thrombosis treatment regimens often necessitate higher thrombolytic dosages over the course of weeks to months[6, 7]. Elevated tPA doses also increase the risk of severe and life-threatening bleeding events[7], such as hemorrhage. Drug delivery systems (DDS) such as nanoparticles, microparticles, and pH-responsive capsules can improve thrombolysis kinetics[8, 9]. While conventional DDS improve stability and circulation, they typically rely on passive diffusion, suffering similarly limited drug penetration issues. Other DDS have utilized molecular targeting strategies, but yield significant systemic side effects[8].

Micro/nanorobots present a minimally invasive solution to thrombus treatment, particularly in small vessels inaccessible to conventional catheters due to size constraints[10, 11]. Given their small scale and enhanced maneuverability, various micro/nanorobotic platforms have been developed as active drug carriers and flow mediators capable of loading and delivering thrombolytics, such as tPA, directly to the clot site[12, 13, 14, 15, 16, 17, 18]. This targeted approach reduces required drug dosages and risk of side effects. Previously, we have demonstrated a high-throughput method for fabricating anisotropic soft microrobot, comprised of encapsulated iron oxide nanoparticles in a hydrogel matrix, which can be manipulated under noninvasive magnetic fields and be programmed to induce collective behaviors[19]. Building upon these findings, we can implement these anisotropic microrobots to thus improve upon existing systemic drug delivery issues.

Here, we show how our HydroBots can enhance thrombolytic efficacy, and its potential for clinical translation. In this work, we conduct extensive structural characterization and *in vitro* biocompatibility evaluations. Through simulation studies, we demonstrate that the proposed HydroBots exhibit enhanced locomotion performance compared to conventional spherical microrobots. Furthermore, *in vitro* validation demonstrated accurate navigation into the no-reflow region and enhanced thrombolytic performance within

a thrombi-on-a-chip system, achieving a tenfold increase in thrombolysis compared to the drug-alone group. Finally, we test the HydroBots in a clinically relevant *in vivo* thrombosis porcine model, where we demonstrate efficacy through convection-mediated thrombolytic delivery **[Fig. 1].**

Results

Lab-Scale HydroBot Manufacturing

A high-throughput droplet-based microfluidic system with a flow-focusing geometry was employed to generate magnetic precursor droplets composed of dextran hydrogel (Mn = 6 kDa) encapsulating magnetic nanoparticles (MNPs). At the flow-focusing junction, the continuous oil phase pinched the aqueous discrete phase, forming droplets through the interplay of hydrophilic and hydrophobic interactions **[Fig. 2A]**. The design of the flow-focusing junction, gradually narrowing down to a 15μm-wide constriction, enabled the controlled formation of small droplets by adjusting the applied pressures.

The water-in-oil precursor magnetic droplet underwent crosslinking via a polyaddition reaction **[Fig. 2A]**, which was initiated by toluene diisocyanate at the droplet interface **[Supplementary Fig. 1]** and further facilitated under a rotating magnetic field (< 10 Hz) produced by a Rotating Halbach Cylinder device. Dipolar interactions aligned the MNPs into bundle configurations within the precursor droplet, assembling into multi-bundles that would compact and align along the HydroBots' major axis **[Fig. 2a]**. Following HydroBot scale-up fabrication and surface functionalization, particle image analysis demonstrated that HydroBots possess a highly uniform ellipsoidal shape **[Fig. 2b]**. Measurements indicated a narrow distribution for both major and minor axes, confirming the consistency in shape and size across the population (major axis: 8 μm, minor axis 4.5 μm) **[Fig. 2c]**.

SEM highlighted the linear and dense dextran network on its surface **[Fig. 2d]**, organized around the multi-bundle structures of the magnetic supra-domain. For a more detailed structural analysis, HydroBot cross-sections were examined using Focused Ion Beam-Scanning Electron Microscopy (FIB-SEM), clearly visualizing the multi-bundle configurations of MNPs within the hydrogel body. To assess the elemental composition and distribution within the HydroBots, we also performed energy dispersive X-ray (EDX) analysis, indicating a homogeneous coverage of carbon and oxygen on the surface of the iron constituents

[Fig. 2d] which was thus illustrated **[Fig. 2e]**, demonstrating its potential for functionalization. We then conducted Fourier Transform Infrared (FTIR) spectrum analysis **[Fig. 2f]** to evaluate HydroBots' chemical composition. Analysis revealed a broad band at 3100 to 3600 cm^{-1}, (O-H stretching from dextran hydroxyl groups), a peak at 2920 cm^{-1} (C-H stretching aliphatic chains), and a peak neat 1700 cm^{-1} (C = O stretching), confirming urethane crosslinking from toluene diisocyanate. Additional peaks at 1440 cm^{-1} and 1250 cm^{-1} indicate aromatic C = C stretching from the same component. Finally, we measured the zeta potential of pure HydroBots and PEGylated HydroBots, enhancing bioadhesion and reducing cell-cell interactions **[Fig. 2g]**. Given no difference with material composition, we proceeded with non-functionalized HydroBots.

In the case of dextran-based microrobots without anisotropy, the low viscosity of dextran enables homogeneous mixing of MNPs, resulting in a uniform distribution within the entire spherical structure. Scanning electron microscopy (SEM) imaging revealed a porous structure within the uniformly dispersed microrobot, suggesting excellent drug-eluting capabilities **[Supplementary Fig. 2a]**. Additionally, EDX analysis confirmed homogeneous surface coverage of carbon and oxygen surrounding the iron constituents, further supporting its uniform composition and structural integrity **[Supplementary Fig. 2b-d]**.

By programming the magnetic supra-domain within the dextran hydrogel body, we observed that the average velocity of HydroBots (23.5μm/s) is nearly five times higher than that of homogeneous microrobots (5.1μm/s) **[Fig. 2h]**, resulting from HydroBot anisotropy due to their overall ellipsoid shape and the multi-bundled structure of their magnetic supra-domain.

Swarm Behavior of HydroBots

As in prior literature[11, 14, 15, 17, 20], we compared the locomotive swarm capabilities of HydroBots compared to homogeneous microrobots in a ring-shaped well structure (5 mg/mL). Under identical magnetic magnitude (20 mT), and their step-out frequencies (10 Hz, homogeneous microrobots; 20 Hz, HydroBots), both types formed wheel-like swarm structures due to dipolar interactions and hydrodynamic effects. However, the HydroBots swarm demonstrated reduced structural stability, due to higher rotation frequency and anisotropic geometry. To quantitatively compare their locomotion performance, the average swarm

velocity was determined. The anisotropic microrobot swarm achieved a higher average velocity (1716 μm/s) than the homogeneous microrobot swarm (820 μm/s) **[Fig. 2i-j, Supplementary Fig. 3]**.

Biosafety Characterization of HydroBots

To validate HydroBots' use in biological settings, we first conducted *in vitro* cytotoxicity tests in human microvascular endothelial cells (HMEC-1) **[Fig. 3a]** and PMA-treated THP-1s, a monocyte cell line differentiated into the M0 macrophage phenotype **[Fig. 3b]**, where we found no change in cell viability up to 24 hours. Similarly, no change in cell viability up to 24 hours was measured in both porcine **[Fig. 3c]** and humans **[Fig. 3d]** peripheral blood mononuclear cells (PBMCs). We then conducted bioadhesion tests on HMEC-1 cells when guiding HydroBots across a cell monolayer with RMF **[Fig. 3e]**, where HydroBots exhibit negligible bioadhesion to HMEC-1s **[Fig. 3f].** Notably, as shown through HMEC-1 immunostaining and fluorescently tagged HydroBots, HydroBots disperse into individual particles upon RMF release, preventing aggregate formation **[Fig. 3g]**. Finally, to confirm that HydroBots' rolling does not induce cell death, we then conducted an immunohistochemical assay on HMECs for HydroBots' cytotoxicity (exposure time 24h and 48h) with minimal caspase-3 staining **[Supplementary Fig. 4a]** and almost all cells having Ki-67 staining **[Supplementary Fig. 4b]**.

HydroBots Exhibit Hemocompatibility and Immunogenicity

Additionally, we assessed HydroBot hemocompatibility with porcine blood by measuring prothrombin time (PT) **[Fig. 3h]**, activated partial thromboplastin time (aPTT) **[Fig. 3i]**, thrombin time (TT) **[Fig. 3j]**, and fibrinogen levels **[Fig. 3k]**, all of which evaluate the extrinsic, intrinsic, and common clotting pathways. The coagulation times and fibrinogen levels were statistically comparable to those observed in the phosphate-buffered saline (PBS) control group, indicating no clotting cascade activation. Hemocompatibility is further confirmed by a negligible hemolysis rate **[Fig. 3l]**.

We then evaluated HydroBot immunogenicity using THP-1 cells differentiated into macrophages (CD68+). Dextran, just like other biomaterial backbones, elicit an immune response when administered into biological settings[21]. Thus, with PBS or 1 μg/mL of lipopolyssacharide (LPS) as a negative and positive control respectively, HydroBots (0.03 or 0.3 mg/mL) do not elicit a significant pro-inflammatory immune

response at 24 **[Fig. 3m]** or 48 hours **[Fig. 3n]** by staining for pro-inflammatory macrophages (CD86+) from CD68+ THP-1 macrophages. Through qPCR, we also determined that only LPS elicited a strong immune response by significant upregulation of IL-6, TNFα and IL-1β at both 24 and 48 hours **[Supplementary Fig. 5a-c]**. We then validated this response through ELISA, which determined that both IL-6 and TNFα concentrations remained constant for HydroBots at 48 hours compared to control **[Fig. 3o-p]**. Finally, we conducted human PBMC immunogenicity studies, which measured no INFγ concentration difference except with phytohemagglutinin (PHA) addition **[Fig. 3q]**, as expected from the literature[22].

Modeling the No-Reflow Region and convection-enhancement induced by rotating HydroBots

For targeted thrombolysis, HydroBots must navigate hemodynamics and into no-reflow regions, typically inaccessible to passive diffusion. We thus designed a Y-bifurcation microchannel model with an artificial blockage to simulate the occluded vasculature. With 95% occlusion in one branch, a pronounced no-reflow region was produced and characterized by near-zero fluid velocity (850 to 0 μm/s) near the blockage **[Supplementary Fig. 6a]**. The drug distribution profile within the no-reflow region suggests low effective therapeutic drug concentrations, resulting from increased channel resistance **[Supplementary Fig. 6b]**. Finally, we modeled the induced convection flow generated by HydroBot administration with a rotating ellipsoid (100 μm, long axis; 50 μm, short axis) immersed in liquid. Velocity profile analysis along a defined cutting line over time showed periodic fluctuations in the surrounding fluid velocity, generating distinct convection flows and enhancing mixing and transport phenomena around the HydroBots. Specifically, the strongest convective flow was observed near the two ends of the ellipsoid **[Supplementary Fig. 7a]**, where velocity peaked at approximately 80 μm/s **[Supplementary Fig. 7b]**.

Establishment of Thrombi-on-a-chip System

Based on the simulation results, we developed a thrombi-on-a-chip system designed as an *in vitro* validation system to evaluate both the locomotion capability of HydroBots within the no-reflow region and their thrombolytic efficacy. The complete system integrated a pressure pump, solution reservoir loaded with HydroBots solution, a Y-bifurcation microfluidic chip, and a magnetic navigation setup compatible with confocal microscopy, enabling real-time visualization of HydroBots responding under an applied magnetic field **[Fig. 4a]**. Our artificial occlusion (PDMS pillar) leading to 95% channel blockage, while ensuring consistent flow resistance conditions, was confirmed using Cy3-labeled nanoparticles to visualize flow profiles. Particle Image Velocimetry (PIV) analysis revealed that flow velocities in the main channel remained comparable to inlet velocities (approximately 850–1000 μm/s) **[Fig. 4b]**. Near the bifurcation point, a no-reflow region was observed with a rapid velocity decrease (850 to 0 μm/s) progressing deeper into the occluded branch. Tracers and active pharmaceuticals could not infiltrate the occluded region **[Supplementary Fig. 8a-b].**

Magnetic Navigation of HydroBots into the No-Reflow Region

Successful navigation of the HydroBot into poorly perfused regions requires overcoming the constraints imposed by minimal or absent flow. To investigate this, simulations were conducted to model and compare the motion interactions of the HydroBot within a no-reflow region **[Supplementary Fig. 9]**. To compare the locomotion capacity of homogenous and HydroBots within the no-reflow region, we performed similar obstructions as before. Without magnetic guidance, all homogenous microrobots bypassed the no-reflow region **[Supplementary Fig. 10a]**. Subsequently, when actuated by a rotating magnetic field (20 mT, 10 Hz, inclination angle 90°, azimuth 45°), homogenous microrobots adjacent to the no-reflow zone overcame the flow drag forces and penetrated the occluded branch at reduced velocities (300 μm/s) **[Supplementary Fig. 10b]**. FITC-labeled HydroBots similarly bypassed the no-reflow region without magnetic actuation **[Fig. 4c]**. However, upon actuation (20 mT, 20 Hz, inclination angle 90°, azimuth 45°) the HydroBots penetrated the no-reflow region **[Fig. 4d-e]**. Due to their anisotropic shape, HydroBots have

a higher step-out frequency, enhancing synchronization with the rotating magnetic field and thus locomotion in low flow environments.

In Vitro *Validation of Enhanced Thrombolysis via Mechanical Interactions and Chemical Lysis*

After demonstrating HydroBots' minimal cytotoxicity, good hemocompatibility, and enhanced locomotion capabilities, we then tested whether HydroBots can be used as effective flow mediator for enhanced thrombolytic efficacy. We first conducted *in vitro* experiments using pure fibrin (10 mm^3) to evaluate fibrin lysis performance of HydroBots using the same Y-junction microfluidic system.

With an out-of-plane RMF (20 mT, 10 Hz), the HydroBots experience a continuous magnetic torque propelling them forward, generating a volumetric net flow towards the no flow region which significantly enhances the penetration and distribution of therapeutic agents into emboli **[Fig. 4f]**. By quantifying the fluorescence intensity of FITC-albumin signal within thrombi, we determined that HydroBot rotation substantially enhances the penetration depth of FITC-Albumin into fibrin emboli (2.65 mm with actuation **[Fig. 4g],** 1.23 mm without actuation), equating to a 115% increase in HydroBot penetration depth compared to the control.

We then tested the drug carrying potential of the HydroBots (5mg/mL) with 0.25% trypsin. Treatment with 0.25% trypsin alone resulted in a thrombolysis rate of 0.11 mm^3/min, with 29% of the fibrin emboli dissolved after 40 minutes. Conversely, with HydroBots and 0.25% trypsin, the artificial fibrin emboli was dissolved within 17.5 min (100% dissolution) with an average lytic rate of 0.57 mm^3/min and a peak rate of 1.15 mm^3/min, nearly tenfold higher than trypsin alone **[Fig. 4h and 4i]**. Mechanical interaction with HydroBots alone produced negligible lysis **[Supplementary Fig. 11]**. We also computed and analyzed the normalized lysis between groups **[Supplementary Fig. 12]** and the real time lysis rate of both groups **[Fig. 4j]**.

During the HydroBot enhanced thrombolytic process, we observed a tendency for the HydroBots clusters to move towards the center of the occluded channel, resulting in an accelerated dissolution of the central region of the emboli. Based on image recognition, we extracted the periphery of the emboli and noted the progressive formation of an inward-concave valley, with the depth of this depression increasing

over time **[Fig. 4k]**. The HydroBot spatial distribution demonstrates the capacity of the HydroBots swarm (indicated in red) into the inner emboli structure (represented in green) throughout lysis **[Fig. 4l]**.

Using FITC-labeled porcine blood clots in a thrombi-on-a-chip system, we found that tPA at 1000 µg/mL produced a 1.5 fold enhancement in lysis kinetics compared to 250 and 500 µg/mL, which showed no significant difference between each other. **[Supplementary Fig. 13]**. Thrombolysis kinetics were then evaluated at varying HydroBot concentrations while maintaining a constant tPA concentration of 1000 µg/mL with a RMF (10 mT, 10 Hz, inclination angle 90°, azimuth 45°). HydroBots significantly accelerated clot lysis compared to tPA alone **[Fig. 4n and 4o]**. Tenecteplase showed thrombolysis kinetics comparable to tPA, while urokinase and streptokinase also benefited from HydroBot addition but to a lesser extent **[Supplementary Fig. 14a–c].** Our results indicate that the HydroBot concentration at 10 mg/mL enhanced the overall thrombolysis rate **[Fig. 4p]**. Overall thrombolysis rates comparing HydroBot-assisted thrombolysis to drug-only treatment demonstrate a 5 to 6-fold increase in the final extent of blood clot lysis in the HydroBot group **[Fig. 4q]**.

In Vivo *Validation of Catheter-Assisted Microrobot Thrombolytic Therapy*

Building on our *in vitro* results, we conducted *in vivo* porcine experiments to evaluate catheter-delivered HydroBot-assisted thrombolysis[10, 12], leveraging the pig's anatomical and physiological similarity to humans[23]. After performing an initial acute cardiac safety study with no adverse effects **[Supplementary Fig. 15a-b]**, we then conducted *in vivo* efficacy studies to determine whether the HydroBots with tPA induced better recanalization **[Fig. 5a-b]**. Using a clinically relevant renal artery thromboembolism model adapted from validated protocols with autologous thrombi[24, 25], we assessed whether HydroBots combined with tPA improved vascular recanalization. Alongside confirming clot size to maximize vessel occlusion **[Supplementary Fig. 16a]**, we validated our model by segmenting the vasculature before and after clot addition and thus measuring the mean maximal length of the vasculature, showing a significant decrease in mean length after clot addition **[Supplementary Fig. 16b]**.

Both kidneys were occluded via administration of *in vitro created* autologous blood thrombi. The magnetic navigation system consists of two permanent magnets mounted on a shaft driven by a DC motor. We simulated the generated RMFs **[Supplementary Fig. 17]** to ensure robust HydroBot navigation to the

occluded vasculature. The setup can create RMFs of around 15 mT at a distance of 7 cm from the surface **[Supplementary Fig. 18]**. The magnetic navigation arm was positioned close to the HydroBot treated kidney to induce an RMF, which rotates the HydroBots towards the occlusion. **[Supplementary Fig. 19a]**. Through catheter administration, one kidney received 100 mg of HydroBots and 15 mg of tPA (n = 3), while the other kidney was administered 15 mg of tPA alone (n = 3) **[Fig. 5c]**. Through automated AI-enhanced fluoroscopy analysis **[Supplementary Fig. 19b]**, HydroBots with 15 mg of tPA exhibited better recanalization via a higher increase in maximum vessel length **[Fig. 5d-f] Supplementary Fig. 20]** and in overall re-perfused vasculature area relative to tPA alone **[Fig. 5f, Supplementary Fig. 21]**, which is due to the significant convective flow enhancement around the blood clot. To confirm convection flow enhancement through HydroBot administration, we also performed a simulation of the drug diffusion in the occluded renal vasculature, which was inspired by our fluoroscopy videos. While the macroscopic drug distribution and flow profiles remain the same regardless of HydroBot administration **[Supplementary Fig. 22]**, HydroBots at the boundary between the clot and stagnant blood demonstrate localized convection, which was enhanced with higher concentrations **[Supplementary Fig. 23]**. Here, this convection-enhanced drug delivery increases the HydroBot concentration and thus thrombolytic efficacy **[Supplementary Fig. 24]**. Keeping the dose of HydroBots constant (100 mg), we also performed a tPA dose response study (1.5 mg, n = 3). However, there was no significant difference in recanalization with less tPA, demonstrating that a sufficient drug dose is required for successful HydroBot-assisted thrombolysis **[Supplementary Fig. 25].**

We sectioned the occluded vessel to confirm the interactions with the blood clot and HydroBots, where we confirmed HydroBot penetration into the thrombus through histology **[Fig. 5g]**. We then evaluated the iron oxide content via magnetic resonance imaging (MRI) to confirm localization, with kidneys with HydroBot administration having higher iron oxide content than control kidneys **[Supplementary Fig. 26]**. We also utilized MRI to perform initial biodistribution studies in various organs **[Supplementary Fig. 27]**, and histology with HydroBots present within the clot alongside its treated kidney, and minimal HydroBots present the control kidney alongside the satellite organs **[Fig. 5i]**.

Discussion

This study presents magnetically programmable anisotropic microrobots (HydroBots) that enhance convection-mediated thrombolytic delivery for treating vascular occlusions. The platform leverages a scalable droplet-based microfluidic fabrication approach using dextran hydrogels, a biocompatible, low-viscosity biomaterial[26] that prevents magnetic nanoparticle aggregation while enabling controlled generation of 5-10 μm diameter microrobots that align with blood cell dimensions for safe microvasculature passage[27]. Magnetic programming transforms these microrobots into anisotropic, ellipsoid structures with multi-bundle magnetic supradomains and pronounced shape anisotropy[19], significantly enhancing locomotion efficiency, step-out frequency, and responsiveness to external rotating magnetic fields under physiological flow conditions[10, 12, 27]. In vitro thrombi-on-a-chip experiments demonstrated that HydroBots operating under out-of-plane rotating magnetic fields (10 Hz) generate volumetric convective flow within no-reflow zones, achieving 5- to 10-fold thrombolytic enhancement when combined with thrombolytic agents with various thrombi through hydrodynamic coupling and flow mediation while exerting minimal mechanical forces on vascular endothelium. Validation in a clinically relevant porcine renal artery occlusion model showed that HydroBot-treated kidneys exhibited approximately 2-fold greater reperfusion than the control group, with significantly enhanced recanalization when combining 15 mg tPA with HydroBots compared to tPA alone, a substantially lower dose than standard systemic thrombolytic regimens[28], and achieved therapeutic outcomes within 30 minutes, faster than catheter-directed thrombolysis[29]. MR imaging and histology confirmed predominant HydroBot localization to the treated kidney with minimal off-target accumulation, supporting the safety profile and magnetic guidance efficacy. This research paves the way for future advancements in magnetically guided micro/nanorobot systems, significantly enhancing thrombus treatment efficacy and patient outcomes. While microrobot technology is still new, this study reflects potential use with thrombolytic enhancement[30, 31]. Given that microrobot technologies are complex and require expertise from various disciplines, further regulatory studies will need to be conducted to ensure safety and efficacy for future translation. Limitations of this work include the need for improved fluoroscopic visibility for real-time clinical tracking and optimized delivery strategies for navigating complex vascular anatomies. Future directions involve refining magnetic actuation protocols to enhance penetration depth in diverse thrombus compositions, developing bioresorbable magnetic formulations to eliminate long-term

foreign body retention, and conducting comprehensive regulatory toxicology and biodistribution studies across larger animal models to facilitate clinical translation of magnetically guided microrobotic thrombolysis systems.

Data Availability

The data that support the findings of this study are available from the corresponding author upon reasonable request.

Author Contributions

All authors contributed to the conceptualization of this manuscript. All authors have reviewed, edited and accepted the final manuscript.

Acknowledgements

This research was performed within the framework of the ETHeart initiative. The authors also gratefully acknowledge the Scientific Center for Optical and Electron Microscopy (ScopeM) for their support and assistance in this work. Y.Y. gratefully acknowledges the support of the China Scholarship Council. Scanning electron microscopy was performed by Ann-Kathrin Seitz with equipment maintained by the Center for Microscopy and Image Analysis, University of Zurich. We would also like to thank Prof. Andrew de Mello for early support in establishing the hydrogel microrobot fabrication, as well as the Nikon Bioimaging Lab Europe for building an AI driven tool to analyze our fluoroscopy images. Cell figures in Figures 3A-D were created with BioRender.com.

Conflict of Interest Disclosure

S.S. is co-founder and member of the board of Magnebotix AG.

Figures

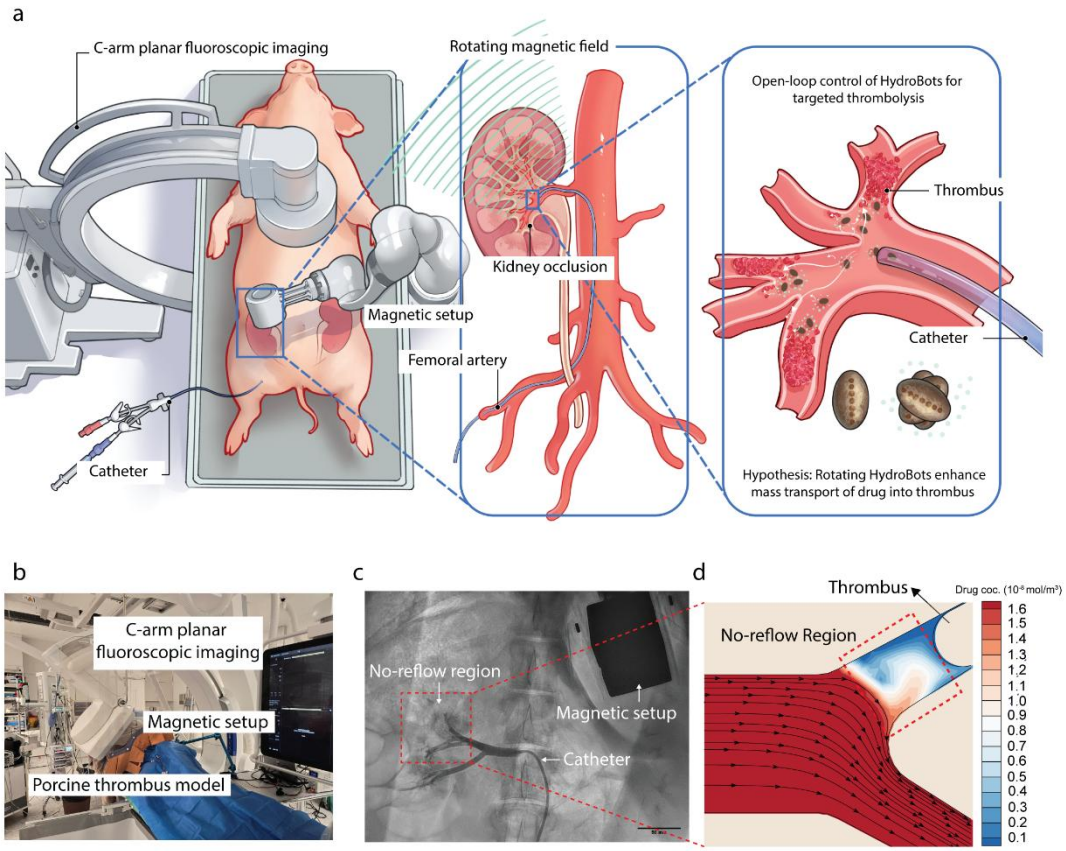

Figure 1. Open Loop Control of HydroBots for Targeted Thrombolysis. (a) Schematic of the experimental setup, including planar fluoroscopic imaging, magnetic setup, and catheter for HydroBots injection. After occluding the kidney by application of autologous thrombi, HydroBots plus thrombolytic are administered, allowing for enhanced thrombolytic delivery. **(b)** Image of surgery suite, with C-arm CT scanner and magnetic setup utilized. **(c)** As indicated with a lack of contrast agent convection, we occlude the vasculature, leading to areas of no-reflow. Fluoroscopy images demonstrate the establishment of a no-reflow region. **(d)** Hydrodynamic simulation results of the no-reflow region. The heatmap signifies drug concentration in the vasculature**,** demonstrating how the no-reflow region limits thrombolytic drug delivery.

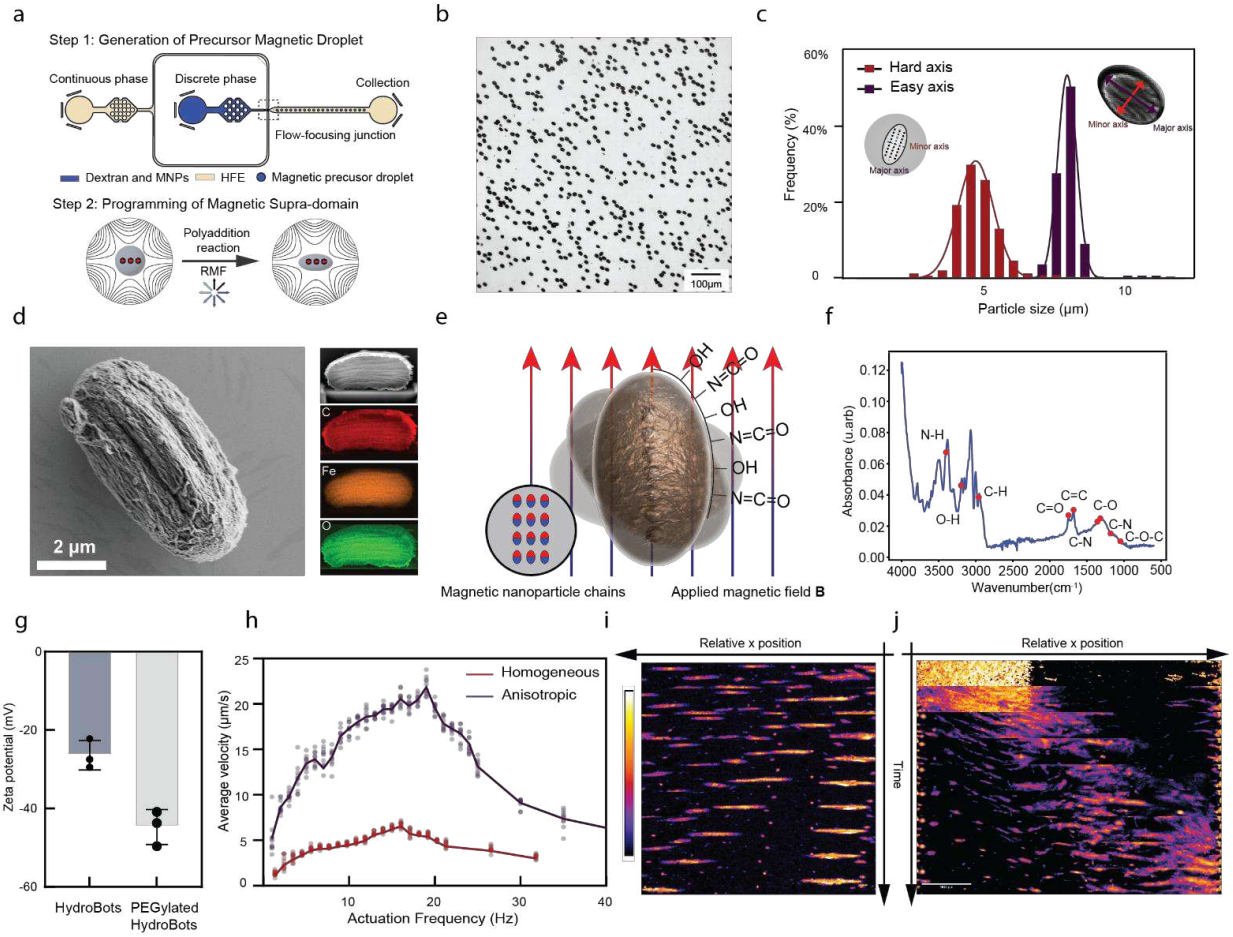

Figure 2. Characterization and quality control of an anisotropic soft hydrogel microrobot (HydroBot). (a) Schematic representation of the laboratory-scale production system for magnetic precursor droplets. Step 1 includes detailed geometry of the flow-focusing droplet-based microfluidic chip, while step 2 shows programming of internal magnetic domains and the overall shape of the HydroBots during the polyaddition reaction within the Halbach cylinder. **(b)** Brightfield image of HydroBots. Scale bar: 100 μm. **(c)** Size distribution of the major and minor axes of the anisotropic HydroBots. **(d)** SEM image of HydroBots. Scale bar: 2 μm. Focused ion beam (FIB) of a sliced hydrobot with corresponding elemental maps (Fe = orange, C = red, O = green). **(e)** Schematic illustration of HydroBot locomotion in an external magnetic field with visualized functional groups. **(f)** FITR spectrum of HydroBots. **(g)** Zeta potential of HydroBots and PEGylated HydroBots. **(h)** Average velocities of homogeneous and anisotropic microrobots as functions of actuation frequency. **(i-j)** Time evolution diagram of microrobot swarm density under out-of-plane RMF for **(i)** homogeneous microrobots and **(j)** HydroBots.

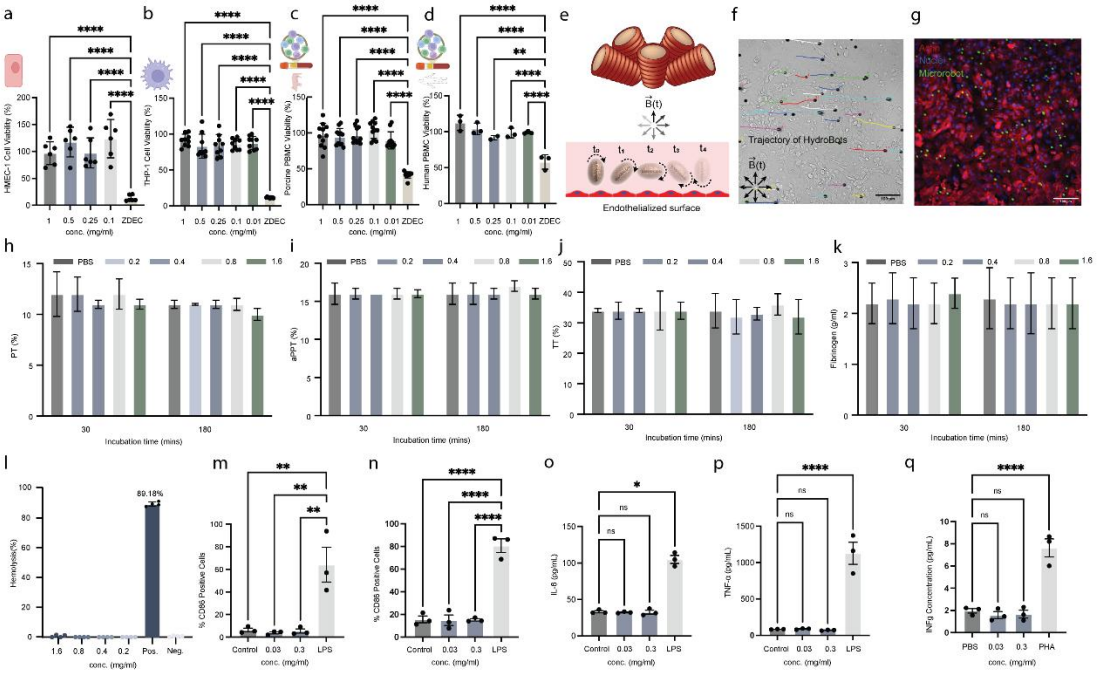

Figure 3. Cytocompatibility, hemocompatibility, and immunogenicity studies indicate HydroBot safety. (a-d) Cytocompatibility in human microvascular endothelial cells (HMEC-1) **(a)** (n = 6 per condition) THP-1-differentiated human macrophages **(b)** (n = 9 per condition), porcine peripheral blood mononuclear cells (PBMCs) **(c)** (n = 9 per condition), and human PBMCs **(d)** (n = 3 per condition), where cell viability was quantified 24 h after treatment with HydroBots via Alamar Blue. Cell viability is reported relative to the untreated control and compared to the positive cytotoxic control, 0.1% zinc diethyldithiocarbamate (ZDEC), with significance calculated using a one-way ANOVA with Dunnett's post-hoc test. Cell icons created in https://biorender.com. **(e)** Schematic illustration of HydroBots' rolling behavior on an endothelial cell monolayer in the presence of a rotating magnetic field. **(f)** Magnetic propulsion of HydroBots on an endothelialized surface. Scale bar: 100 μm. **(g)** Representative fluorescent microscopy image shows microrobots (green) rolling along the surface of HMEC cells (red, actin). Scale bar: 100 μm. **(h-k)** Hemocompatibility of HydroBots were evaluated by measuring prothrombin time (PT) **(h)**, activated partial thromboplastin time (aPTT) **(i)**, thrombin time (TT) **(j)**, and fibrinogen levels **(k)**, essential for clot formation, to evaluate bleeding risk (n = 3 replicates per HydroBot dose (0.2-1.6 mg/mL)). **(l)** Hemolytic response of the HydroBots, with Triton X-100 as the positive control and polyethylene glycol as the negative control. N = 4 replicates per condition. **(m-n)** Immunostaining analysis for CD86+ THP-1-derived macrophages that were exposed to HydroBots (0.03 or 0.3 mg/mL), PBS or LPS (1 μg/mL) at 24 h **(m)** and 48 h **(n).** N = 3 per condition. **(o-p)** Downstream IL-6 **(o)** and TNFα **(p)** ELISA of cell media, where THP-1 cells were exposed to HydroBots (0.03 or 0.3 mg/mL) with PBS as the negative control and lipopolysaccharide (LPS) at 1 μg/mL as the positive control. N = 3 per condition. **(q)** INFγ ELISA of cell media, where human PBMCs were exposed to HydroBots (0.03 or 0.3 mg/mL) with PBS as the negative control and 2% phytohemagglutinin (PHA) as a positive control. N = 3 per condition.

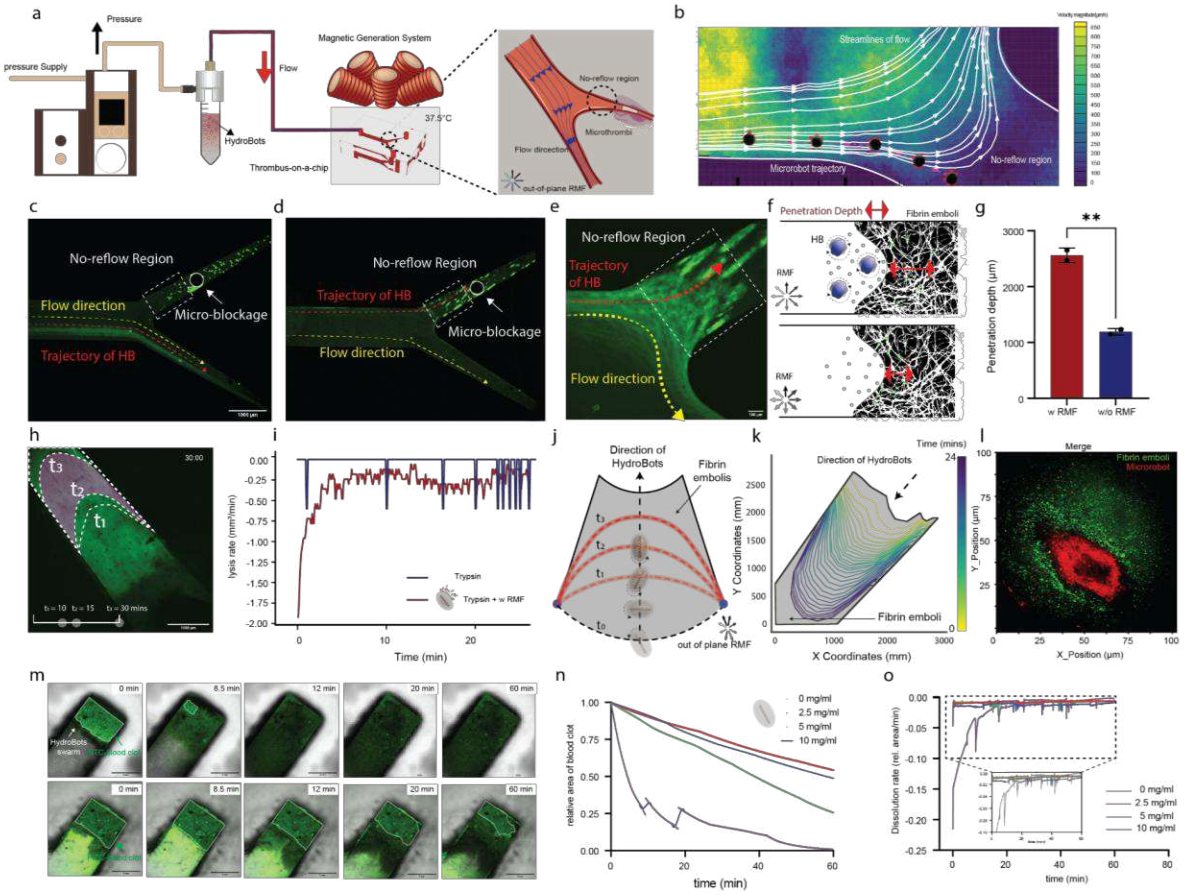

Figure 4. HydroBots demonstrate enhanced locomotion activity towards thrombi and *in vitro* thrombolytic efficacy. (a) Experimental setup for the in vitro assessment of the no-reflow region. **(b)** PIV analysis illustrates the flow profile within the no-reflow region and the complete navigation process of the individual HydroBot infiltrating the no-reflow region. **(c)** Time-lapse images of Hydrobots drifting with the flow direction and bypassing the no-reflow region. **(d)** Time-lapse images of actuated HydroBots being steered into the no-reflow region. **(e)** Zoomed-in view of the HydroBots' trajectory within the no-reflow region under RMF. **(f)** Convection-enhanced drug delivery though HydroBots, and passive drug diffusion into the thrombi. **(g)** Quantification of penetration depth within fibrin emboli with actuated HydroBots vs. nonactuated HydroBots. **(h)**Fluorescent images of targeted lysis by HydroBots at different time points. **(i)** Changes of the real time lysis rate of fibrin emboli over time. **(j)** Overview of the fibrin emboli lysis process with the HydroBots. **(k)** Visualization of shape changes during fibrin emboli lysis. **(l)** Spatial distribution of the HydroBots within blood clot during the lysis process. **(m)** Timelapse of thrombi dissolution with 10 mg/mL HydroBots and 1 mg/mL tPA (top), and 1 mg/mL tPA (bottom). **(n)** Thrombolysis kinetics of blood clots created through ($CaCl_2$ 2.5%) incubated with various concentrations of HydroBots. **(o)** Comparison of blood clot lysis as the first derivative of **(n)** using different HydroBots concentrations with t-PA.

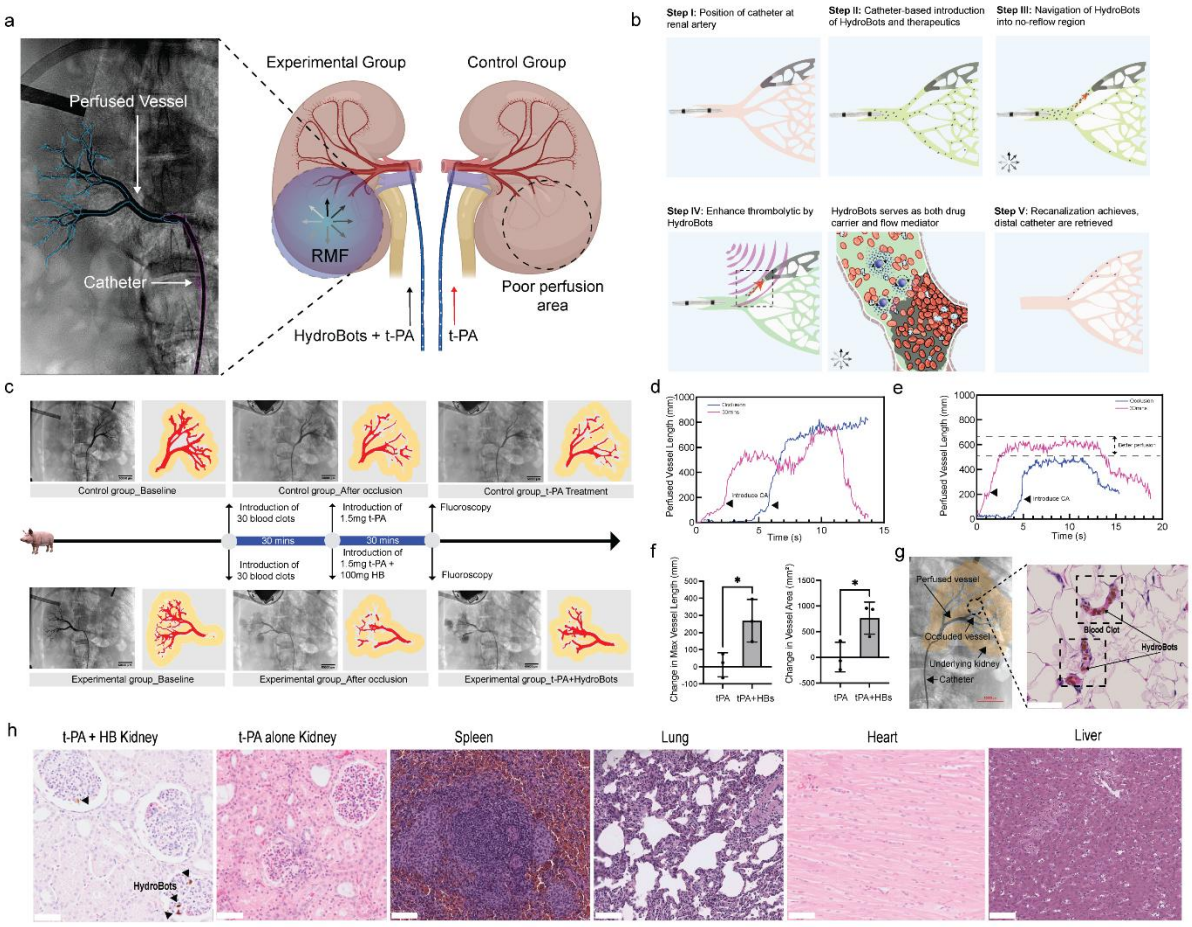

Figure 5. HydroBots enhance thrombolysis in a porcine thrombosis model. (a) Overview of experimental setup with renal artery occlusion model, treatment groups, and example fluoroscopy. **(b)** HydroBot enhanced thrombolysis overview within *in vivo* studies. **(c)** Experimental timeline for efficacy studies with AI-enhanced segmentation performed by Nikon Imaging. **(d-e)** Time lapsed vessel segmentation of the underlying renal vasculature for both 15 mg alteplase treatment alone **(d)** at post occlusion and post 30 minutes treatment **(d)**, and 100 mg HydroBots and 15 mg alteplase treatment alone at post occlusion and post 30 minutes treatment **(e)**. **(f)** The change in maximum vessel length and change in vasculature area were quantified by calculating the difference in the maximum vessel length and vasculature area 30 minutes post treatment and post occlusion. Significance was determined by an unpaired student's t-test. **(g)** Overview of fluoscopic image with labelled occluded and perfused vasculature and catheter. Scale bar: 5 cm. Representative H&E images of the occluded vasculature containing HydroBots embedded in the clot. Scale bar: 50 μm. **(h)** Representative H&E images of a kidney treated with 15 mg t-PA and 100 mg HydroBots, and a kidney treated with 15 mg t-PA alone. Scale bar: 50 μm. Representative H&E histology of the spleen, lung, heart, and liver demonstrating no microrobot retention up to 4 hours post-administration. Scale bar: 100 μm. n = 3 replicates for 15 mg alteplase, n = 3 replicates for 15 mg alteplase and 100 mg HydroBot.

Materials and Methods

High Throughput Fabrication of HydroBots

HydroBots were prepared following a similar protocol to the one described previously, with the modification of substituting PEGDA19 with dextran. This change was implemented due to dextran's lower viscosity, which significantly reduced the aggregation of MNPs. Briefly, magnetic precursor droplets were formed using a high-throughput droplet-based microfluidic device fabricated by soft lithography techniques. The microfluidic chip design included distinct inlets for the continuous phase (HFE 7500, 3M, USA) and discrete phase (dextran-MNPs solution), a flow-focusing junction with a width of 15 μm for droplet formation, and an outlet for HydroBots collection. The microfluidic chip also incorporated widened channels and integrated pillar structures designed to filter debris from raw material, thereby preventing clogging of the flow-focusing region.

For droplet generation, the continuous phase consisted of HFE 7500 supplemented with 1% surfactant (008-FluoroSurfactant-5wtH-200G, RAN Biotechnologies, USA), while the discrete phase comprised Dulbecco's phosphate-buffered saline (DPBS, ThermoFisher) mixed with 8% w/v dextran (molecular weight 6000) and 20% magnetic nanoparticle solution (EMG-700, Ferrotec, USA). At the flow-focusing junction, the continuous phase exerted pressure on the discrete phase, leveraging the hydrophobic and hydrophilic interactions between the two phases to achieve uniform and continuous droplet formation. Flow pressures of both phases were adjusted according to the desired HydroBot size, with droplets being collected into an Eppendorf tube.

Crosslinking of the magnetic precursor droplets was initiated by the incremental addition of a crosslinking solution, consisting of one part toluene diisocyanate (TDI) mixed with 42 parts HFE, at a volume four times that of the dextran-MNP solution used. Subsequently, the droplets were placed inside a Halbach cylinder rotating at 5 Hz for 22 hours. After this period, an additional portion of the crosslinking solution was added dropwise, and the droplets were further incubated in a thermal shaker set to 24°C and 300 rpm for an additional 22 hours. Finally, the formed HydroBots were purified by sequential washing in clean HFE, treatment with 5% perfluorooctanol (PFO) in HFE for 5 minutes, followed by successive washes in ethyl acetate, ethanol, and PBS, before ultimately being resuspended in PBS.

HydroBot Characterization Techniques

The size distribution of HydroBots was determined by analyzing brightfield images captured in the imaging chamber, applying an appropriate threshold, and performing size analysis using Fiji software. Surface morphology was examined through scanning electron microscopy (SEM) using a Zeiss Merlin instrument equipped with a Gemini II column (ScopeM). Fourier Transform Infrared (FTIR) spectroscopy was conducted to evaluate the molecular composition and structural characteristics of the samples. Dynamic Light Scattering (DLS) was performed to measure the zeta potential of the HydroBots, indicating their surface charge properties. Additionally, Focused Ion Beam (FIB) analysis provided insights into the internal component distribution and structural cross-section of the HydroBots. Prior to characterization, all HydroBots were sequentially washed three times each with ethyl acetate, ethanol, and deionized (DI) water, followed by resuspension in DI water. Samples intended for SEM, FIB, and FTIR analyses were further lyophilized overnight to ensure complete dehydration and preservation of structural integrity.

Convection Flow Simulations

We implemented a two-dimensional transient simulation in COMSOL Multiphysics® to investigate convection flow induced by a rotating magnetic ellipsoidal particle. The model combined multiple physics interfaces: Laminar Flow to solve the Navier–Stokes equations for incompressible viscous fluid around the ellipsoid, Solid Mechanics to define the rigid ellipsoid body and prescribe rotational motion and Moving Mesh to accommodate mesh deformation and rotation without compromising quality. Magnetic actuation was simulated using the Magnetic Fields, No Currents interface, applying a uniform magnetic field to generate torque that drives ellipsoid rotation. The rotational motion was imposed through Solid Mechanics and coupled with the moving mesh to synchronize deformation across domains.

The workflow involved creating an ellipsoid geometry (100 μm major axis, 40 μm minor axis) embedded in a large fluid domain. Independent meshing was applied to the rotating ellipsoid and stationary fluid region, with identity pairs maintaining continuity at the interface. Physics coupling was achieved using Multiphysics nodes to link flow, mesh motion, and rigid body rotation. A time-dependent solver was configured, beginning with a stationary initial solution to establish baseline conditions, followed by transient

analysis with time steps chosen to capture rotational dynamics and flow development. Post-processing included evaluation of velocity fields, streamlines, and vorticity to characterize induced convection, with parametric sweeps over angular velocity to assess its influence on flow behavior.

Mammalian Cell Culture

Human microvascular endothelial cells-1 (HMEC-1, CRL-3243) were purchased from the American Type Culture Collection (ATCC, USA) and cultured in T-75 flasks. The culture medium consisted of MCDB 131 (Gibco, USA) supplemented with epidermal growth factor (EGF, 10 ng/mL), 20% fetal bovine serum (FBS, Biowest, France), hydrocortisone (1 µg/mL, Sigma Aldrich), L-glutamine (10 mM, Gibco, USA), and 1% penicillin-streptomycin (P/S, Gibco, USA). Cultures were maintained under standard incubation conditions at 37°C in a humidified environment with 5% CO_2.

Upon reaching approximately 80% confluency, cells were either passaged for further propagation or prepared for experimental applications. Appropriate cell densities for subculturing and experimentation were determined using a hemacytometer. For detachment, confluent cell monolayers were rinsed with phosphate-buffered saline (PBS), followed by incubation with 3 mL of 0.25% trypsin (Gibco, USA) at 37 °C and 5% CO_2 for 6 minutes. Once detached, trypsin activity was halted by adding 6 mL of fresh supplemented MCDB 131 medium, and the resulting cell suspension was transferred into a 15 mL centrifuge tube. Cells were centrifuged at 600 × g for 5 minutes, after which the supernatant was discarded. The pellet was then resuspended in 1 mL of fresh supplemented medium, and cell concentration was adjusted using a hemacytometer for subsequent experimental use.

THP-1 cells were purchased from the American Type Culture Collection (ATCC, USA) and cultured in T25 and T75 flasks in RPMI-1640 GlutaMax medium (Gibco, USA), supplemented with 10% fetal bovine serum (FBS, Biowest, France) and 1% penicillin-streptomycin (P/S, Gibco, USA). Cultures were maintained under standard incubation conditions at 37 °C in a humidified environment with 5% CO_2. Upon reaching approximately 80% confluency, cells were either passaged for further propagation or prepared for experimental applications. Appropriate cell densities for subculturing and experimentation were determined using a hemacytometer. Cells were centrifuged at 600 × g for 3 minutes, after which the supernatant was

discarded. The pellet was then resuspended in 1 mL of fresh supplemented medium, and cell concentration was adjusted using a hemacytometer for subsequent experimental use.

Porcine peripheral blood mononuclear cells (PBMCS) were isolated from porcine whole blood via density gradient centrifugation with SepMate (Stemcell) tubes and LymphoPrep (Stemcell) density gradient medium. Blood was first diluted 1:1 with PBS, and added to the SepMate Tubes containing LymphoPrep. Tubes were then centrifuged at 1200 × g for 10 minutes and the top layer containing enriched PBMCs was transferred into a new tube. Subsequently, PBMCs were washed twice with PBS. PBMC were then immediately plated in a 96 well plate for later experimental studies, with appropriate cell densities determined via hemacytometer.

Human PBMCs were purchased from StemCell Technologies (USA), and cultured in T75 flasks in RPMI-1640 GlutaMax medium, supplemented with 10% fetal bovine serum (FBS, Gibco) and 1% penicillin-streptomycin (P/S, Gibco, USA). Cultures were maintained under standard incubation conditions at 37 °C in a humidified environment with 5% CO_2. One day post thawing, cells were then prepared for experimental applications, with appropriate cell densities determined via hemacytometer.

Macrophage Differentiation

Upon reaching approximately 80% confluency, THP-1s were then seeded into either a 12 well plate for downstream immunogenicity experiments or a 96 well plate for cytocompatibility experiments. All cells were seeded with 400 ng/μL phorbol 12-myristate 13-acetate (PMA) for 3 to 4 days to stimulate macrophage differentiation into M0 macrophages. Cells were left for 3-4 days to achieve macrophage differentiation, which was determined by visualizing cell adherence.

Cytocompatibility Experiments

HMEC-1, M0 macrophage differentiated THP-1, porcine PBMCs, and human PBMCs were used for cytocompatibility experiments. Both cell types were seeded into 96 well plates (ThermoFisher) at a density of 12’800 cells per well in serum free media (HMEC-1: MCDB-1 with 1% P/S; THP-1: RPMI-1640 with 1% P/S) and left overnight. THP-1 cells were then differentiated into M0 macrophages by 400 ng/μL PMA stimulation for 3 days. Once acclimated, all cell types were treated with HydroBots of various

concentrations (0.01 to 1 mg/mL) alongside 0.1% zinc diethyldithiocarbamate as a control for cytotoxicity and PBS as a negative control. Viability was measured 24 hours later through Alamar Blue (ThermoFisher, USA), and read 3 hours later on a plate reader (Tecan) at 570 nm for absorbance. Percentage viability was determined by normalizing to PBS treated cells.

Macrophage Immunogenicity Studies

Upon reaching approximately 80% confluency, THP-1s were seeded into a 12 well plate for downstream immunogenicity experiments, and were differentiated into macrophages as mentioned previously. For immunogenicity experiments, quantitative PCR (qPCR), immunostaining, and ELISAs were conducted to evaluate the macrophage specific response to HydroBot administration. All experiments were conducted with 0.33 mg/mL and 0.03 mg/mL HydroBots, with 1 μg/mL LPS and PBS as positive and negative controls for immunogenicity.

Using a Qiagen RNeasy Isolation Kit (ThermoFisher), RNA was isolated from 12 well plates of THP-1 derived macrophages and were quantified on a NanoDrop spectrophotometer (ThermoFisher). RNA was then converted to cDNA using the SuperScript IV protocol (ThermoFisher), with qPCR done via TaqMan primers for the following genes: IL6 (Hs00174131_m1), TNF (Hs00174128_m1), and IL1B (Hs01555410_m1), with 18S (Hs01375212_g1) and GAPDH (Hs02786624_g1) used as housekeeping genes. Relative gene expression was evaluated by calculating $\Delta\Delta C_t$ to the housekeeping gene[32].

Immunostaining was performed using 12 well plates of THP-1 derived macrophages. Cells were fixed in 4% paraformaldehyde (ThermoFisher) for 15 minutes. All groups were then blocked with 10% goat serum for 1 hour, and then treated with both rabbit anti-CD86 antibody and mouse anti-CD68 antibody for 1 hour. Samples were then treated with goat anti-rabbit Alexa Fluor 488 antibody and goat anti-mouse Alexa Fluor 568 antibody for 30 minutes. Finally, samples were then treated with 1μg/mL DAPI for 10 minutes, were coverslipped, and imaged on a Nikon Ti2 Eclipse confocal microscope. Images were then evaluated by calculating the total number of CD86+ cells among CD68+ macrophages.

A M1/M2 Cytokine ELISA (Arigo Bio, Taiwan), assaying for IL-4, IL-6, IL-10, and TNFα, was performed with the media of 12 well plates of THP-1 derived macrophages (n = 3 technical replicates). The Pierce BCA Protein assay (ThermoFisher) was done to determine the total protein concentration in the

media. The manufacturer's protocol was followed, with the plate assayed on a Tecan plate reader, and each cytokine concentration was normalized to the total protein concentration.

PBMC Immunogenicity Studies

Human PBMCs were seeded into either 12 well plates or 96 well plates for downstream immunogenicity studies. For immunogenicity studies in 12 well plates, qPCR and ELISAs were conducted to measure lymphocyte activation in response to HydroBot administration. All experiments were conducted with 0.33 mg/mL and 0.03 mg/mL HydroBots, with 1 μg/mL LPS and phytohemagglutinin (PHA) also used for general immune cell activation and T-cell activation respectively. PBS was used as an unstimulated control. PBMCs were treated for 24 hours, and then used for downstream experiments.

RNA was isolated from the 12-well plates of PBMCs and was quantified as done previously for THP-1s. Conversion to cDNA and qPCR were done similarly to THP-1 experiments, with primers for the following genes: IL6 (Hs00174131_m1), TNF (Hs00174128_m1), and IL1B (Hs01555410_m1), with 18S (Hs01375212_g1) and GAPDH (Hs02786624_g1) used as housekeeping genes.

An IFNγ ELISA (ThermoFisher, USA) was performed with the media of 12 well plates containing PBMCs using HydroBots at 0.03 and 0.3 mg/mL, alongside phytohemagglutinin (PHA) as a positive control. Protein concentrations were quantified as done previously for THP-1s. The manufacturer's protocol for the IFNγ ELISA was followed, with each replicate's concentration quantified through non-parametric least squares fit. The plate was read 3 hours later on a plate reader (Tecan) at 450 nm for absorbance.

Immunohistochemical Viability Assay

HMEC-1 cells were seeded at a density of 30,000 cells/cm² and cultured overnight in 1 mL of fresh medium in a humidified incubator. Subsequently, the medium was removed and replaced with fresh medium containing varying concentrations (500 μg/mL, 250 μg/mL, and 125 μg/mL) of PEGylated HydroBots and non-functionalized HydroBots. A negative control (medium alone) and a positive control (1 μM staurosporine) were included in parallel. Cells were incubated with these treatments in a total volume of 1 mL medium for 24 hours under standard culture conditions (37 °C, 5% CO_2).

After treatment, cells were rinsed three times with DPBS, fixed using 4% buffered formalin, and stored at 4 °C until further analysis. Cell proliferation was evaluated by immunostaining for the proliferation marker Ki67 (clone MIB-1, monoclonal mouse anti-human antibody, Dako/Agilent GA62661-2, USA). Apoptosis was assessed using immunostaining for cleaved caspase-3 (polyclonal rabbit anti-human antibody, Cell Signaling Technology 9661, Switzerland). Immunohistochemical staining was carried out on formalin-fixed cells utilizing an automated immunohistochemistry system at the Department of Surgical Research, University Hospital Zürich, Switzerland.

Hemolytic Assessments

The hemolytic assay was adapted from the method previously described by Barry W. Neun[33]. Whole porcine blood was stored at 4 °C and utilized within 24 hours after pooling. Porcine hemoglobin standards (Sigma-Aldrich, USA) were combined with Drabkin's solution (Sigma-Aldrich, USA) to prepare calibration standards at concentrations of 0.80, 0.40, 0.20, 0.10, 0.05, and 0.025 mg/mL, alongside quality control samples at concentrations of 0.625 and 0.125 mg/mL. Plasma-free hemoglobin (PFH) was obtained by centrifuging the porcine blood at 800 × g for 15 minutes. Total blood hemoglobin (TBH) samples were prepared by mixing 20 µL of whole blood with 5 mL of Drabkin’s solution.

Subsequently, 200 µL of each calibration standard and control sample, as well as 100 µL of PFH, were dispensed in duplicate into a 96-well plate. Each well was diluted by adding an additional 100 µL of Drabkin's solution. The plate was gently shaken for 1 to 2 minutes, and the absorbance was measured at a wavelength of 540 nm. The hemoglobin content in the samples was calculated by comparison with the calibration curve.

The remaining whole blood was adjusted to a hemoglobin concentration of 10 mg/mL by dilution with DPBS. For the hemolysis assay, 100 µL of this diluted blood was combined with 700 µL DPBS and 100 µL of the respective HydroBot concentrations prepared in DPBS. Controls included a blank sample (DPBS only), a positive control (Triton X-100), and a negative control (polyethylene glycol, MW 8000). All

samples were incubated in a water bath maintained at 37 °C for 3 hours, with gentle mixing every 30 minutes. After incubation, the samples were centrifuged at 800 × g for 15 minutes. From each sample, 100 µL of the resulting supernatant was transferred to a new 96-well plate and further diluted with 100 µL of Drabkin's solution. A fresh calibration curve and corresponding quality controls were prepared simultaneously. Finally, the absorbance of each sample was recorded at 540 nm to assess hemolysis, where percent hemolysis was calculated by determining the hemoglobin concentration per well and dividing that value by the hemoglobin concentration in whole blood, then multiplying by 100.

Anticoagulation Evaluation

Anticoagulant activity was evaluated *in vitro* by measuring activated partial thromboplastin time (aPTT), prothrombin time (PTT), thrombin time (TT), and fibrinogen levels (FIB) at four different HydroBot concentrations (0.2, 0.4, 0.8, and 1.6 mg/mL). To achieve these concentrations, 50 µL of each HydroBot solution was mixed individually with 2.7 mL of freshly collected porcine blood, which was used within 4 hours of collection. The mixtures were then incubated under gentle agitation (40 rpm) in a humidified incubator maintained at 37 °C with 5% CO_2. At specific incubation intervals (30 and 180 minutes), samples were centrifuged at 2000 × g for 10 minutes at 20 °C to isolate plasma. The plasma samples were subsequently analyzed for coagulation parameters at the Department of Medical Oncology and Hematology, University Hospital Zürich, Switzerland.

Thrombi-on-a chip Microsystem Design

We developed two distinct thrombi-on-a-chip systems to investigate different aspects of HydroBot functionality. The first microsystem was designed to evaluate the maneuverability of HydroBots within the no-reflow region. This setup consisted of a pressure pump (Fluigent, Germany) connected to a Y-bifurcation microfluidic chip featuring symmetrically narrowing branches, fabricated using soft lithography techniques. Instead of using real blood clots, artificial pillars with a radius of 50 µm and a height of 200 µm were employed to simulate the no-reflow region, ensuring consistent flow resistance across experiments. A 2

wt.% polyvinylpyrrolidone (PVP) solution was used to replicate the viscosity of blood while minimizing interference with imaging. The PVP solution, mixed with HydroBots, was infused at approximately 1 mm/s to mimic physiological arteriole flow conditions. The microfluidic chip was placed on an integrated imaging system (Nikon Ti2 Eclipse) combined with a magnetic manipulation setup (MFG-100-i, MagnebotiX).

For in vitro evaluation of HydroBot-induced thrombolysis, a larger microfluidic chip with an open-top design was utilized to facilitate consistent placement of clot at a fixed location. The channel molds were designed in Siemens NX 10 and exported as STL files. The main channel measured 1000 μm in width and 1500 μm in length, with depths of 1500 μm and 500 μm in specified sections. Two symmetrical branches, each 1400 μm long and 600 μm wide, extended from the main channel. The designs were fabricated using an AnyCubic MonoX digital light printer with Prima Creator “Super Strong” black resin. Following isopropanol cleaning, a two-part silicone (Mold Max XLS II, Smooth-On) was cured around the printed parts to create reusable molds. These molds were then used to cast clear epoxy replicas (EpoxAcast 690, Smooth-On). To reduce PDMS adhesion, the cured epoxy molds underwent oxygen plasma treatment followed by chlorotrimethylsilane vapor deposition under vacuum. The molds were subsequently rinsed with isopropanol and dried with nitrogen prior to use. Polydimethylsiloxane (PDMS) was prepared by mixing silicone elastomer base and curing agent at a 10:1 weight ratio. After centrifugation at 1000 × g for 5 minutes, the mixture was poured into epoxy molds, degassed for 30 minutes, and cured at 80 °C for 24 hours. The cured PDMS components were oxygen plasma-treated and bonded to glass slides, then baked at 120 °C overnight to ensure strong adhesion. Blood clots, formed as described below, were introduced into one branch of the microsystem at a predetermined location to obstruct flow. A solution of Alteplase or a combination of HydroBots with Alteplase was then perfused through the channel. Prior to Alteplase administration, porcine plasma was introduced. The fibrinolysis process was monitored in real-time using confocal microscopy to assess clot size reduction.

Fabrication of Autologous Thrombi

Porcine blood anticoagulated with citrate was obtained from the animal facility at the University Hospital of Zurich (USZ) and stored at 4°C prior to use. To initiate clot formation within the thrombi-on-a-chip system, whole blood was mixed with calcium chloride solutions at concentrations of 2.45% or 10%

(w/v) in a volume ratio of 9:1. For better visualize the lysis process, fluorescein isothiocyanate (FITC) fibrinogen (ThermoFisher) was pre-mixed with whole blood at a 1:20 volume ratio to produce FITC-labeled clots. The microfluidic chips were plasma cleaned for 30s, before the mixture was added into the no-reflow section of the chip. A plastic stopper was added to the rest of the chip to obstruct blood flow to this region. This mixture was then incubated at 37°C for 6 min to promote activation of the coagulation cascade and facilitate clot development at the fixed position within the microfluidic chip.

PIV Analysis of No-Reflow Region

Red fluorescent nanoparticles (FluoSpheres carboxylated microspheres) were incorporated into the PVP solution and the PVP-HydroBots suspension at a concentration of 0.5% (v/v) relative to the manufacturer's stock solution. HydroBots were prepared at a concentration of 1 mg/mL for these experiments. Samples were infused into the thrombi-on-a-chip system at a controlled flow velocity of 1 mm/s and positioned within the integrated magnetic actuation setup.

Fluorescence time-lapse imaging was performed to capture the motion of the fluid under various experimental conditions. The resulting image sequences were processed using PIV analysis, implemented through the PIVlab toolbox in MATLAB. PIVlab employs cross-correlation algorithms to track the displacement of fluorescent nanoparticles between successive frames, enabling accurate quantification of local fluid velocity fields. PIV approach provided spatial and temporal resolution of flow dynamics within the microfluidic device, facilitating quantitative assessment of HydroBot-induced fluid motion.

Computational Fluid Dynamics (CFD) Analyses

Numerical simulations of laminar flow and drug transport within the occluded vessel were performed using COMSOL Multiphysics. The geometry of the Y-bifurcation microchannel was created in AutoCAD and subsequently imported into COMSOL for analysis. The simulations employed the Laminar Flow module to solve the Navier-Stokes equations governing steady-state, incompressible, laminar flow within the microfluidic domain.

To model passive drug transport within the no-reflow region, the Transport of Diluted Species module was utilized, simulating the convection and diffusion of t-PA. The drug transport was governed primarily by convection and molecular diffusion, with the diffusion coefficient set to 5×10^{-11} m²/s, consistent with literature values for t-PA. The initial concentration of t-PA was specified as 16.764×10^{-9} mol/m³. A multiphysics coupling function linked the laminar flow and species transport modules, allowing for simultaneous solution of fluid velocity and concentration fields to accurately capture the interaction between flow dynamics and drug diffusion. Simulation results, including velocity profiles and concentration distributions, were exported from COMSOL and visualized using TecPlot 360 to facilitate detailed post-processing and interpretation.

Simulation of Particle Interaction within No-Reflow Region

We employed the lattice Boltzmann method (LBM) to investigate particle motion within the no-reflow region by solving the quasi-incompressible Navier-Stokes equations governing fluid flow. The primary objective was to determine whether the particle could penetrate into the no-reflow area. The LBM lattice spacing and time step were set to $\Delta x = 1$ and $\Delta t = 1$, respectively. An ellipsoidal colloid with axis ratios of a:b:c = $8\Delta x : 4\Delta x : 4\Delta x$ (equivalent to 8:4:4) was used as the model particle.

The ellipsoid was positioned at three distinct locations along the streamline adjacent to the no-reflow region under pure pressure-driven flow, which corresponds to the boundary of the reflow region. All three positions were set near the boundary of the channel, with the ellipsoid center located $3\Delta x$ above the surface. Additionally, a spherical particle placed at the position 2 was included to examine the influence of particle shape on motion. Particle dynamics were driven by an external magnetic field, with rotational frequency (ω) and field orientation (θ) varied systematically to fully characterize particle behavior. The angle θ is defined as the angle between the normal vector to the plane of the external magnetic field and the horizontal negative direction. The baseline parameters were set to $\omega\Delta t = 0.005$ and $\theta = 60°$, from which a parameter sweep was conducted. To normalize the system behavior, two dimensionless quantities were introduced: the dimensionless $t^* = \frac{t}{T} = \frac{\omega t}{2\pi}$ and the dimensionless velocity $v^* = \frac{v}{vi} = \frac{v}{\omega 0 R}$, where $w_0 = 0.005$ the standard angular velocity and R=6 is the radius of the equivalent sphere corresponding to the ellipsoid.

Magnetic Navigation Setup for In Vivo Porcine Experiments

We used a rotating permanent magnet-based system for in vivo experiments. The magnetic field is generated by two 50.8 x 50.8 x 25.4 mm N40 magnets (Q-51-51-25-N, supermagnete). The magnets are mounted on a shaft that is driven by a brushless DC motor (MMS742038-24-R1-1, EZmotion). A 3D-printed PLA casing houses the magnets and the motor. The casing is mounted on a mechanical arm (McMaster-Carr) that allows for flexible positioning. We controlled the setup with a laptop running software (MotionLAB, EZmotion) to adjust the rotation frequency.

In Vivo Thrombolysis

The animal study was approved by the local Committee for Animal Experimental Research (Cantonal Veterinary Office Zürich, Switzerland) under the license number ZH072/2023. All animals were intact females with body weights (BW) of 75-85 kg. To guarantee the absence of infectious diseases with a possible impact on the cardiovascular system, standard vaccination strategies against Hemophilus parasius, porcine circovirus 2, porcine parvovirus, Erisypelothrix rhusiopathiae, and Escherichia coli were implemented by the breeder. Upon arrival at the facility, all animals were visually examined regarding their general behavior, posture and gait, skin color, breathing pattern, appetite, and fecal and urinary excretion. If abnormalities were observed, a physical examination was additionally conducted. Each animal was guaranteed a minimum acclimatization period of 7 days before the experiment. A total of 7 animal studies were conducted, with 1 biosafety study, and 6 renal occlusion studies with vascular occlusions created at the left and right main renal artery.

On the day of the experiment, animals were sedated with an intramuscular injection of ketamine (Ketasol®-100 ad us.vet.; Dr. E. Graeub AG, Berne, Switzerland; 15mg/ kg BW), azaperone (Stresnil® ad us.vet.; Elanco Tiergesundheit AG, Basel, Switzerland; 2mg/ kg BW), and atropine (Atropinsulfat KA 1%; Kantonsapotheke, Zurich, Switzerland; 0.05mg/ kg BW). Anesthesia was then induced by administration of propofol (Propofol ® Lipuro 1%; B. Braun Medical AG, Sempach, Switzerland; 1-2mg /kg BW) in an

intravenous line introduced in the V. auricularis until the swallowing reflex was repressed and intubation was possible. Anesthesia was maintained with a combination of constant intravenous infusion of propofol (Propofol ® Lipuro 2 %; B. Braun Medical AG, Sempach, Switzerland; 3 mg/kg BW/h) and inhalation of isoflurane (Attane™ Isoflurane ad.us.vet.; Piramal Enterpr. India; 1.0-1.5%) in 70 % oxygen:air mixture using mechanical ventilation. Insertion of a urinary catheter and monitoring urine production as well as performing repeated blood gas analysis allowed conclusions on fluid loss during anesthesia, which was compensated by constant infusion of Ringer's solution (Ringerfundin®; B. Braun Medical AG, Sempach, Switzerland; 5-10ml/kg BW/h). For pain relief, all pigs received intravenous injections of buprenorphine (Temgesic®; Indivior Schweiz AG, Baar, Switzerland; 0.01 mg/kg BW) every 5h throughout the course of the experiment. Invasive blood pressure measurements were performed through a central arterial line.

First, the acute biosafety of HydroBots was evaluated following direct administration into the coronary artery (n = 1). During the initial biosafety trial, continuous electrocardiogram (ECG) monitoring was performed, and ischemic cardiac biomarkers were measured to evaluate potential myocardial injury. Blood samples were collected at 60, 120, and 180 minutes following the intervention.

Before occlusion, blood collection was done to establish baseline readings for hematocrit, white blood cell count, fibrinogen levels, clotting time. Blood samples were stored at room temperature until analysis in the clinical laboratory at the University Hospital of Zurich (Switzerland). Whole blood was also collected and clotted for 30 minutes in a 50 mL conical at 25°C to create autologous blood clots for renal occlusion. The clotted whole blood was excised out and manually cut into 10 cm pieces, with approximately 30 large autologous blood clots introduced into the renal artery via catheter for 1 hour to cause occlusion. At random, one kidney was picked for alteplase and microrobot treatment, while the other kidney was treated with alteplase alone. In the experimental group, 1.5 mg or 15 mg of alteplase was administered simultaneously with HydroBots (100 mg per 10 mL, 10 mg/mL) in 10 mL aliquots every 10 min for a total of 30 mL over the course of 30 min, with a magnet setup positioned near the thrombus to enable magnetic targeting. For the alteplase-only control group, either a 1.5 mg (n = 3) or 15 mg (n = 3) dose of alteplase was administered in 10 mL aliquots every 10 min, for a total of 30 mL over the course of 30 minutes. For simultaneous treatment, we administered both the experimental and control groups via two separate

catheters to their respective kidneys. After treatment, iodine contrast agents were administered via catheter 30 minutes post treatment to monitor blood flow restoration via fluoroscopy.

Post-experiment, organs were harvested, photographed, and preserved individually in formalin containers for further histological evaluation. Prior to MRI imaging, organs were rinsed multiple times to remove formalin residue. For sample preservation, spleen, lung, liver, heart, muscle, and kidneys were cut into 3cm^3 cubes, and placed into multiple histology cassettes per organ, including. Samples intended for frozen storage were embedded in optimal cutting temperature (OCT) compound and transferred to a -80°C freezer for long-term storage.

Modeling Convective Drug Transport with In Vivo Renal Vasculature

COMSOL Multiphysics 6.2 was used as a finite element method (FEM) to analyze the fluid flow, microrobot motion and drug distribution inside the Realistic pig artery vasculature model. All the simulation is performed in two-dimensional space to reduce computational cost. The pig artery vascular image is obtained from the real image of the CT and author manually draws the vascular model using NX 10 software. In COMSOL, the fluid flow interface was employed to solve the equations governing incompressible non-Newtonian physiological flow. The solid mechanics interface was employed to solve the motions of microrobots governed by external magnetic field. The fluid structure interaction interface is employed to describe the interaction between microrobots and fluid. The moving mesh (ALE) is employed to handle large deformation due to the microrobot movement. The transport of diluted species interface was used to solve the transport equation for the drugs. The medium inside the channel without blood clot area was defined to be blood and this medium was modeled by the Carreau model, whereas the blood clot area was modeled as the same condition with blood excluded as it has high viscosity and thus no shear flow in the no-flow region.

In CFD analyses, we solve momentum and continuity equations for an incompressible flow:

$$\nabla \cdot \sigma = 0, \qquad \nabla \cdot u = 0$$

Where u is the fluid velocity, $\sigma = -pI + \tau$ is the stress tensor, and p and τ are the pressure and the viscous shear stress. To capture the shear-thinning behaviors, we used the Carreau model[34], as previously used for blood.

$$\eta = \eta_\infty + (\eta_0 - \eta_\infty)(1 + \lambda^2|\dot{\gamma}|^2)^{n-1/2}$$

Where η_0 and η_∞ are zero- and infinite-shear rate viscosities, $\dot{\gamma} = \nabla u + (\nabla u)^T$ is the strain-rate tensor, the power-law index n characterizes the degree of shear thinning (n < 1, n = 1 is Newtonian fluid), and $1/\lambda$ is the critical shear rate where the non-Newtonian fluid behavior becomes significant[35]. In this study, we listed parameter values in **Supplementary Table 1**, related to blood properties[36].

For arteries, pulsatile flow was applied. The flow pulsatility was tuned according to the Womersley number (W_o)[37].

$$W_o = \left(\frac{D}{2}\right)\left(\frac{\omega\rho}{\mu}\right)^{0.5}$$

For CFD simulations done in the study, D is the diameter of the vessel, ω is the angular frequency of the oscillations, ρ, and μ are the density and dynamic viscosity of the fluid, which is $\rho = 1100kgm^{-3}$ and $\mu = 3.5cP$, Womersley numbers of 3.5 were used for arteries[38]. The pulsatility function was defined as follows[39]:

$$V_{flow}(t) = \bar{V}_{flow} \times \left(1 + Asin(\omega t) - Acos(2\omega t)\right)$$

where $\bar{V}_{flow}$ is the average flow speed **[Supplementary Table 1]**, *t* is the time step, and *A* defines the amplitude of the waves.

The HydroBot motion is attributed to an external rotating magnetic field, fluid flow and dipole interaction forces. Here, external rotating magnetic field induces moment:

$$\tau = m \times B$$

The external magnetic field was implemented as a spatially uniform rotating magnetic field, applied identically to all HydroBots with field gradients not considered:

$$B = B_0 \cos(2\pi f t)\, \hat{e}_x + B_0 \sin(2\pi f t)\, \hat{e}_y$$

where m is magnetic moment of HydroBots and B is external magnetic field. B_0 is magnetic field intensity, and *f* is actuation frequency.

The dipole interaction forces between HydroBots were defined as:

$$F_{dip}(i) = \frac{3\mu_0}{4\pi} \sum_{\substack{j=1 \\ j \neq i}}^{N} \frac{\mathbf{m_i m_j}}{\mathbf{r_{ij}^4}} \left[\left(1 - 5\left(\hat{m} \cdot \hat{r}_{ij} \right)^2 \right) \hat{r}_{ij} + 2\left(\hat{m} \cdot \hat{r}_{ij} \right) \hat{m} \right]$$

Where μ_0 is the magnetic permeability of free space, $\mathrm{m_i}$ the strength of the dipole moment of the i[th] particle, $\hat{\mathrm{m}}$ is the unit vector of the magnetic field, $\mathrm{r_{ij}}$ is the distance between the centers of the ith and jth particles, and $\hat{\mathrm{r}}_{\mathrm{ij}}$ the unit vector of the corresponding two-particle chain axis. The dipole interaction forces are only considered when the distance between two microrobots is smaller than 8d.

The excluded-volume force is implemented to prevent mesh overlapping of HydroBots[40]:

$$F_{ev}(i) = 2\frac{3\mu_0}{4\pi(\mathbf{R_c})^4} \sum_{\substack{j=1 \\ j \neq i}}^{N} m_i m_j e^{-\xi\left(\frac{\mathbf{r_{ij}}}{2\mathbf{R_c}} - 1\right)} \hat{r}_{ij}$$

where R_c is the minimum separated distance between microrobots. Here, numerical simulations are performed with ξ = 30. Using this value for ξ in a configuration where two dipoles aligned with the magnetic field are separated by a distance of 2.2R_c, the corresponding excluded volume force acting on a single microrobot is 14 times smaller than the opposing magnetic attraction force. Thus, its influence on isolated dipoles is negligible.

For fluid flow boundary conditions, a laminar velocity profile with an average magnitude $\underline{V_{flow}}$ was assumed at the inlet, constant pressure was assumed at the vessel outlet, and all walls were modeled as no-slip boundaries. For boundary conditions applied to the transported species, a constant NP (drug) concentration of 1mol/m^3 was set as the inflow condition, while a general outflow boundary condition was employed at the outlet, and boundary condition setup consistent with the purpose of elucidating effects of convective transport for particles inside the blood clot.

Here, our assumption was consistent with the expected dominance of convective transport for particles inside the blood clot. The diffusion coefficient in the blood clot was thus decided as $D = 2.7 \times 10^{-13} m^2 s^{-1}$ for nanoparticles (NP) based on the experimental data about collagen gels found in literature[41] and diffusion coefficient of NP in blood was decided as $6.2753 \times 10^{-13} m^2 s^{-1}$ using the Stokes-Einstein Equation[42].

Magnetic Resonance Imaging

Ex-vivo magnetic resonance imaging on treated kidneys and satellite organs was performed on a clinical 1.5 T system (AmbitionX, Philips Healthcare, Best, the Netherlands). T2*-mapping was performed using a 3D multi-echo gradient echo sequence with the following parameters: FOV 190/3707/51mm^3, resolution 1.3×1.3×1.3mm^3 reconstructed to 0.83×0.83×1.3mm^3, TR/TE/echo spacing 29/2.8/1.4ms, 18 echoes, flip angle 20°, SPIR fat saturation and 4 signal averages. T2* as well as R2* maps were computed online by the scanner software.Presence of Hydrobots was indicated by localized T2* shortening in the T2* maps.

Fluoroscopy Analysis

Fluoroscopic imaging was used to assess renal artery recanalization before and after treatment for both kidneys in all *in vivo* trials. Images were acquired at the time of complete occlusion (baseline), and 30 minutes post-treatment. To visualize perfused vasculature, an iodine-based contrast agent (Ultravist 300) was administered, and fluoroscopic frames were selected during peak contrast passage through non-occluded vessels. To minimize variability between users, the same investigator administered contrast agent and acquired images across all *in vivo* trials.

The Nikon Bioimaging Lab Europe developed an automated, AI-enhanced workflow for fluoroscopy analysis (Supplementary Figure X). In brief, fluoroscopy files were first converted to TIFF format using Fiji ImageJ, and then imported into NIS-Elements. Using file metadata, time-lapse step and XY resolution were set to 66 ms and 391 µm/px, respectively. Nikon's AI-based denoising tool (Denoise.ai) was applied to improve image quality prior to segmentation.

For vein segmentation (red section), an AI-based segmentation model (Segment_ai) was trained on selected frames manually traced from fluoroscopy images. Segment_ai generated a preliminary binary mask of the vein. The catheter region was segmented separately using catheter_AI, and gaps in both vein and catheter masks were closed using a morphological CircularClose operation. A composite maximum intensity binary of the vein (veinMax) was obtained using BinStackOr, followed by circular closing and

selection of the largest object to exclude spurious signals. The vein binary was then refined by filtering to retain only objects present within the veinMax mask. To approximate the kidney outline and further reduce false positives, veinMax was dilated by 25 pixels to create a preliminary kidney binary. This dilation served as a spatial exclusion region, acknowledging that it approximates rather than precisely defines renal boundaries. Binary post-processing included noise removal, morphological closing, and the use of BinStackOr2 to generate a unified binary mask applicable across all time frames. Largest object selection was used to remove false positives.

Catheter segmentation (purple section) employed a second AI model (SegmentObjects_ai) trained on four selected single frames depicting the empty catheter, as previously described. This step was designed to exclude the catheter from downstream quantification but did not require precise dimensional accuracy, given that catheter metrics were not quantified.

Quantitative measures were derived from the refined binaries. Parameters including area, length of binary regions, and image intensity under each binary mask were computed for every frame. Temporal aggregation of measured parameters was performed to generate time-lapse profiles. All outputs were exported as comma-separated value files, with the maximum vessel area and the maximum vessel length calculated per animal and compared between treatment.

We also analyzed our data with manual segmentation. As with image acquisition, all image analyses were performed under identical display and scaling conditions to minimize variability. At each timepoint, representative fluoroscopy images were extracted and analyzed using Fiji ImageJ. The perfused vasculature was manually delineated by tracing contrast-filled vessel regions using image analysis software. Only vessels visibly perfused with contrast agent were included in the analysis as regions without detectable contrast signal were considered non-perfused and excluded. The total area of contrast-perfused vasculature was quantified for each fluoroscopy video by calculating the enclosed area of the traced regions. In addition, the distance from the tip of the catheter to the most perfused microvasculature was calculated, constituting the maximum length of the vasculature. Finally, blood stasis was quantified by the enhanced contrast present post contrast administration. Both the maximum length and area were thus represented as a percent change compared to the occlusion. Manual image segmentation was performed

by one investigator blinded to treatment condition and time point. To assess segmentation reproducibility, a subset of images was independently traced by a second investigator, and agreement between tracings was evaluated using inter-rater comparison of measured vascular area. Where applicable, repeated tracings were averaged for subsequent analysis.

Immunohistochemistry of Tissue Blocks

After formalin fixation for at least 24 hours at room temperature, the biopsies were dehydrated and embedded in paraffin. Prepared sections with a thickness of 3 μm were stained with hematoxylin (Artechemis, Zofingen, Switzerland) and eosin (Waldeck, Germany) and then digitized with a slide scanner (Olympus, Hamburg, Germany). Imaging was performed with equipment maintained by the Center for Microscopy and Image Analysis (ZMB), University of Zürich (Switzerland), and on an Olympus VS200 slide scanner (Olympus, Netherlands). Digital images of representative fields were captured, and analyses were performed using QuPath software (Version 0.5.1.).

Statistical Analysis

All data were expressed as mean ± SEM. For comparisons between two groups, an unpaired student's T-test was performed. One way analysis of variance (ANOVA) followed by a Tukey's post-hoc test was used for comparisons between multiple groups, except for cytocompatibilty tests which used a one way ANOVA followed by a Dunnett's post-hoc test. Kolmogorov-Smirnov test was used to compare the distributions of histograms or line plots. All statistical analyses were performed in GraphPad Prism V10. Significance levels were indicated as not significant (ns), $P > 0.05$; *$P \leq 0.05$; **$P < 0.01$; ***$P < 0.001$; and ****$P < 0.0001$.

References:

1. Stark K, Massberg S. Interplay between inflammation and thrombosis in cardiovascular pathology. *Nature Reviews Cardiology* **18**, 666-682 (2021).

2. Yau JW, Teoh H, Verma S. Endothelial cell control of thrombosis. *BMC Cardiovasc Disord* **15**, 130 (2015).

3. Alkarithi G, Duval C, Shi Y, Macrae FL, Ariëns RAS. Thrombus Structural Composition in Cardiovascular Disease. *Arteriosclerosis, Thrombosis, and Vascular Biology* **41**, 2370-2383 (2021).

4. Mackman N, Bergmeier W, Stouffer GA, Weitz JI. Therapeutic strategies for thrombosis: new targets and approaches. *Nature Reviews Drug Discovery* **19**, 333-352 (2020).

5. Rezkalla SH, Kloner RA. No-Reflow Phenomenon. *Circulation* **105**, 656-662 (2002).

6. Walie BE, Hagemeyer CE, Xu R, Niego Be. Thrombolytic drugs for ischemic stroke: historical perspective, state of play, and future developments. *Journal of Thrombosis and Haemostasis*, (2025).

7. Cox C, Roberts LN. Basics of diagnosis and treatment of venous thromboembolism. *Journal of Thrombosis and Haemostasis* **23**, 1185-1202 (2025).

8. Chen A, Mesfin JM, Gianneschi NC, Christman KL. Intravascularly Deliverable Biomaterial Platforms for Tissue Repair and Regeneration Post-Myocardial Infarction. *Advanced Materials* **36**, 2300603 (2024).

9. Zenych A, Fournier L, Chauvierre C. Nanomedicine progress in thrombolytic therapy. *Biomaterials* **258**, 120297 (2020).

10. Nelson BJ, Pané S. Delivering drugs with microrobots. *Science* **382**, 1120-1122 (2023).

11. Zhang B, Jiang X. Magnetic Nanoparticles Mediated Thrombolysis-A Review. *IEEE Open J Nanotechnol* **4**, 109-132 (2023).

12. Landers FC*, et al.* Clinically ready magnetic microrobots for targeted therapies. *Science* **390**, 710-715 (2025).

13. Xie M*, et al.* Bioinspired Soft Microrobots with Precise Magneto-Collective Control for Microvascular Thrombolysis. *Advanced Materials* **32**, 2000366 (2020).

14. Yang M*, et al.* Swarming magnetic nanorobots bio-interfaced by heparinoid-polymer brushes for in vivo safe synergistic thrombolysis. *Science Advances* **9**, eadk7251 (2023).

15. Wang B*, et al.* tPA-anchored nanorobots for in vivo arterial recanalization at submillimeter-scale segments. *Science Advances* **10**, eadk8970 (2024).

16. Wang Z, Klingner A, Magdanz V, Misra S, Khalil ISM. Soft Bio-Microrobots: Toward Biomedical Applications. *Advanced Intelligent Systems* **6**, 2300093 (2024).

17. Wang Q*, et al.* Untethered miniature robots for minimally invasive thrombus treatment: From bench to clinical trials. *The Innovation* **6**, (2025).

18. Bao H, Zhang S, Luo J, Meng J, Wang S. Thrombus Boring Microrobot Prepared by an Integrated Phase Separation and Interfacial Self-Assembly Process Toward Thrombolysis. *Angewandte Chemie International Edition* **64**, e202503221 (2025).

19. Yan Y*, et al.* Programming structural and magnetic anisotropy for tailored interaction and control of soft microrobots. *Communications Engineering* **3**, 7 (2024).

20. Jiang J, Yang L, Zhang L. An Overview of Micro/Nanorobot Swarm Control: From Fundamental Understanding to Autonomy. *IEEE/ASME Transactions on Mechatronics* **30**, 2338-2354 (2025).

21. Sharma S, Jagadeesh Chandra Bose K. Biomedical Applications of Dextran. In: *Biopolymers for Biomedical Applications*) (2024).

22. Chang SH*, et al.* The synergistic effect of phytohemagglutinin and interferon-gamma on the expression of tumor necrosis factor-alpha from RAW 264.7 cells. *Immunol Lett* **98**, 137-143 (2005).

23. Cesarovic N, Lipiski M, Falk V, Emmert MY. Animals in cardiovascular research: Clinical relevance and translational limitations of animal models in cardiovascular medicine. *European Heart Journal* **41**, 200-203 (2020).

24. Cesarovic N*, et al.* Development of a Translational Autologous Microthrombi-Induced MINOCA Pig Model. *Circulation Research* **133**, 291-293 (2023).

25. Tang X*, et al.* Synergistic Integration and Pharmacomechanical Function of Enzyme-Magnetite Nanoparticle Swarms for Low-Dose Fast Thrombolysis. *Small* **18**, 2202848 (2022).

26. Lanvers P, Broeker J, Schmid J. Clinical-type dextran: A review on process and enzyme engineering strategies to control molecular weight distribution. *Carbohydrate Polymers* **364**, 123783 (2025).

27. Wang Q*, et al.* Untethered miniature robots for minimally invasive thrombus treatment: From bench to clinical trials. *The Innovation* **6**, 100874 (2025).

28. Broderick JP, Hacke W. Treatment of Acute Ischemic Stroke. *Circulation* **106**, 1563-1569 (2002).

29. Fleck D, Albadawi H, Shamoun F, Knuttinen G, Naidu S, Oklu R. Catheter-directed thrombolysis of deep vein thrombosis: literature review and practice considerations. *Cardiovasc Diagn Ther* **7**, S228-s237 (2017).

30. Nelson BJ, Kaliakatsos IK, Abbott JJ. Microrobots for minimally invasive medicine. *Annu Rev Biomed Eng* **12**, 55-85 (2010).

31. Wrede P, Remlova E, Chen Y, Deán-Ben XL, Sitti M, Razansky D. Synergistic integration of materials in medical microrobots for advanced imaging and actuation. *Nature Reviews Materials*, (2025).

32. Livak KJ, Schmittgen TD. Analysis of relative gene expression data using real-time quantitative PCR and the 2(-Delta Delta C(T)) Method. *Methods* **25**, 402-408 (2001).

33. Neun BW, Ilinskaya AN, Dobrovolskaia MA. Updated Method for In Vitro Analysis of Nanoparticle Hemolytic Properties. *Methods Mol Biol* **1682**, 91-102 (2018).

34. Bird RB, Armstrong RC, Hassager O. *Dynamics of polymeric liquids. Vol. 1, 2nd Ed. : Fluid mechanics*. John Wiley and Sons Inc.,New York, NY; None (1987).

35. Chen Y, Demir E, Gao W, Young YN, Pak OS. Wall-induced translation of a rotating particle in a shear-thinning fluid. *Journal of Fluid Mechanics* **927**, R2 (2021).

36. Shibeshi SS, Collins WE. The Rheology of Blood Flow in a Branched Arterial System. *Appl Rheol* **15**, 398-405 (2005).

37. Womersley JR. Method for the calculation of velocity, rate of flow and viscous drag in arteries when the pressure gradient is known. *J Physiol* **127**, 553-563 (1955).

38. Fung YC. *Biomechanics: Circulation*. Springer New York (2013).

39. Sherwin S, Blackburn H. Three-dimensional instabilities of steady and pulsatile axisymmetric stenotic flows. *Journal of Fluid Mechanics* **533**, 297-327 (2005).

40. Gao Y, Hulsen MA, Kang TG, den Toonder JMJ. Numerical and experimental study of a rotating magnetic particle chain in a viscous fluid. *Physical Review E* **86**, 041503 (2012).

41. Ramanujan S, Pluen A, McKee TD, Brown EB, Boucher Y, Jain RK. Diffusion and convection in collagen gels: implications for transport in the tumor interstitium. *Biophys J* **83**, 1650-1660 (2002).

42. Dill K, Bromberg S. *Molecular Driving Forces: Statistical Thermodynamics in Biology, Chemistry, Physics, and Nanoscience*. CRC Press (2010).

Supplementary Files

This is a list of supplementary files associated with this preprint. Click to download.

- SupplementaryInformation.pdf